

# Real-Space Imaging of Two-Dimensional Antiferromagnetism on the Atomic Scale

S. Heinze,<sup>1,2</sup> M. Bode,<sup>1\*</sup> A. Kubetzka,<sup>1</sup> O. Pietzsch,<sup>1</sup> X. Nie,<sup>2</sup>  
S. Blügel,<sup>2</sup> R. Wiesendanger<sup>1</sup>

A two-dimensional antiferromagnetic structure within a pseudomorphic monolayer film of chemically identical manganese atoms on tungsten(110) was observed with atomic resolution by spin-polarized scanning tunneling microscopy at 16 kelvin. A magnetic superstructure changes the translational symmetry of the surface lattice with respect to the chemical unit cell. It is shown, with the aid of first-principles calculations, that as a result of this, spin-polarized tunneling electrons give rise to an image corresponding to the magnetic superstructure and not to the chemical unit cell. These investigations demonstrate a powerful technique for the understanding of complicated magnetic configurations of nanomagnets and thin films engineered from ferromagnetic and antiferromagnetic materials used for magnetoelectronics.

Nanomagnetism, or the understanding and design of complex multicomponent magnetic nanostructures, is one of the current frontiers in magnetism. Research in this field is fueled by interesting fundamental physics as well as the technological importance of these structures to the magnetic data-storage industry (1) and the cutting-edge field of magnetoelectronics (2). Driven by the motivation of applying the exchange bias effect (3) to tune the device characteristics in giant-magnetoresistance elements, strong efforts are currently being made to study antiferromagnetic (AFM) films adjacent to ferromagnetic ones (4, 5). This arrangement gives rise to a wide variety of complex magnetic structures, e.g., antiferromagnetism, spin-density waves, and frustrated spin-structures, that determine the magnetic structure at the surfaces of thin films. Surface-sensitive techniques that combine high spatial resolution ( $\leq 10$  nm) in real-space with a sufficient degree of magnetic sensitivity could provide a great deal of insight into these phenomena. Unfortunately at present, such techniques are not routinely available. This is the reason why, for example, domain boundaries or two-dimensional (2D) antiferromagnetism is poorly understood. The ultimate lower limit of a 2D AFM is a magnetic monolayer (ML) of chemically equivalent atoms, where adjacent atoms at nearest-neighbor sites have magnetic mo-

ments with opposite directions, deposited on a nonmagnetic substrate. More than 10 years ago, Blügel *et al.* (6) predicted the existence of such 2D antiferromagnets, such as V, Cr, and Mn on noble-metal substrates, on the basis of first-principles calculations. However, experimental verification of this is a scientific challenge because the antiferromagnetism is at the atomic scale, the total magnetization is zero, and the Néel-temperature  $T_N$  is unknown. Although there have been a variety of attempts to verify that antiferromagnetism in these structures exists and some supporting evidence (7) has been reported, unambiguous proof is still required.

We demonstrate the potential of spin-polarized scanning tunneling microscopy (SP-STM) to unravel complex magnetic superstructures with atomic resolution. In particular, we report SP-STM images of a 2D AFM prepared as a thin film, one ML thick, of chemically identical Mn atoms grown pseudomorphically on W(110). We found that non-spin-polarized tunneling electrons image the chemical surface unit cell without any magnetic contribution, whereas spin-polarized electrons probe the change in translational symmetry due to the magnetic superstructure, which gives rise to a different image corresponding to the respective magnetic structure. In agreement with first-principles calculations, the AFM configuration is described as a checkerboard arrangement of Mn atoms with magnetic moments of opposite direction and an easy axis of the magnetization oriented in the film plane, and the STM image exhibits a stripe pattern rather than a diamond pattern.

We initially investigated the electronic, structural, and magnetic properties of a pseudomorphic Mn ML on W(110), theoret-

ically using the first-principles (8, 9) full-potential linearized augmented plane wave (FLAPW) method within the spin-polarized local density approximation (LDA) (10). Three possible magnetic configurations were considered: ferromagnetic (Fig. 1A),  $c(2 \times 2)$ -AFM (Fig. 1B), and  $p(2 \times 1)$ -AFM (Fig. 1C). For all of them, the equilibrium interlayer distance between Mn and W was determined by total energy minimization. By comparing the total energies of the three magnetic structures, we conclude that the  $c(2 \times 2)$ -AFM configuration (Fig. 1B) is the magnetic ground-state structure, i.e., at low temperatures the magnetic moments of adjacent nearest-neighbor atoms will point in opposite directions. The energy of the  $c(2 \times 2)$ -AFM configuration is 100 and 70 meV per Mn atom lower than the ferromagnetic (Fig. 1A) or  $p(2 \times 1)$ -AFM (Fig. 1C) state, respectively. The spin-orbit interaction added to the calculations favors the magnetic moments of the  $c(2 \times 2)$ -AFM structure to have an in-plane orientation along the  $[1\bar{1}0]$  direction (long side of the surface unit cell). The energy difference between the in-plane and out-of-plane orientation of the magnetic moment, known as the magnetocrystalline anisotropy energy, amounts to about 1.3 meV per atom.

The SP-STM has been explored by Wiesendanger *et al.* (11, 12). In the working principle (Fig. 2), the electronic structure of Mn is expressed in terms of spin-dependent local density of states (DOS)  $n_{\uparrow(\downarrow)}$ . Because a Mn atom is magnetic, the DOS of majority,  $n_{\uparrow}$ , and minority,  $n_{\downarrow}$ , electrons (insets in Fig. 2) around the Fermi energy,  $E_F$ , which is relevant for the tunneling of electrons, is different and the spin-polarization,  $P = (n_{\uparrow} - n_{\downarrow})/(n_{\uparrow} + n_{\downarrow})$ , is nonzero. However, the sum of both,  $n_o = n_{\uparrow} + n_{\downarrow}$ , is identical above any Mn atom, so a non-spin-polarized STM measurement will only be sensitive to the chemical unit cell. If the STM tip can be made sensitive to the spins of the tunneling electrons—for example, by coating the STM-tip with Fe or Gd—the tunneling current  $I$  depends on the angle  $\theta$  of the relative orientation between the magnetization axes of tip and sample as well as on the electronic structure and on the spin-polarization  $P_S$  and  $P_T$  of the sample (Mn) and the tip states, respectively. We can decompose the tunneling current into two contributions,  $I(\theta) = I_o + I_p \cos\theta$ , the conventional tunneling current of non-spin-polarized electrons  $I_o$ , and the additional contribution  $I_p$  due to the tunneling of spin-polarized electrons,  $I_p \sim P_S P_T$  (in the limit of small applied bias voltage  $V$ ). Obviously, the highest effect is expected where tip and sample magnetization are either parallel or antiparallel, whereas the effect vanishes for a perpendicular geometry.

According to conventional wisdom, spin-polarization is a small effect, and one might

<sup>1</sup>Institute of Applied Physics and Microstructure Research Center, University of Hamburg, Jungiusstrasse 11, D-20355 Hamburg, Germany. <sup>2</sup>Institut für Festkörperforschung, Forschungszentrum Jülich, D-52425 Jülich, Germany.

\*To whom correspondence should be addressed. E-mail: bode@physnet.uni-hamburg.de

expect normal STM images to be slightly modulated because of magnetism. Instead, it is quite different. The STM image of a periodic surface, i.e., the change  $\Delta I$  of the tunneling current  $I$  as a function of the lateral position  $\mathbf{r}_{\parallel}$  of the tip, can be written in terms of a 2D Fourier expansion

$$\Delta I(\mathbf{r}_{\parallel}, z, \theta, V) = \sum_{n \neq 0} I_{G_{\parallel}^n}(z, \theta, V) \exp(iG_{\parallel}^n \mathbf{r}_{\parallel}) \quad (1)$$

$G_{\parallel}^n$  denotes the reciprocal lattice vectors and  $I_{G_{\parallel}^n}(z, \theta, V)$  is the tip-sample distance- ( $z$ ), angle- ( $\theta$ ), and bias-voltage ( $V$ )-dependent expansion coefficient. Because of the tunneling of electrons through the vacuum barrier, these coefficients decrease exponentially with increasing length  $G_{\parallel}^n$ , and to a good approximation, the topographic STM image is determined by the smallest nonvanishing reciprocal lattice vectors  $G_{\parallel}^{(1)}$  (13)

$$\Delta I(\mathbf{r}_{\parallel}, z, \theta, V) \approx I_{G_{\parallel}^{(1)}}(\theta, V) \exp(iG_{\parallel}^{(1)} \mathbf{r}_{\parallel}) \times \exp \left[ -2z \sqrt{2m/\hbar^2 |E_F + eV| + (G_{\parallel}^{(1)}/2)^2} \right] \quad (2)$$

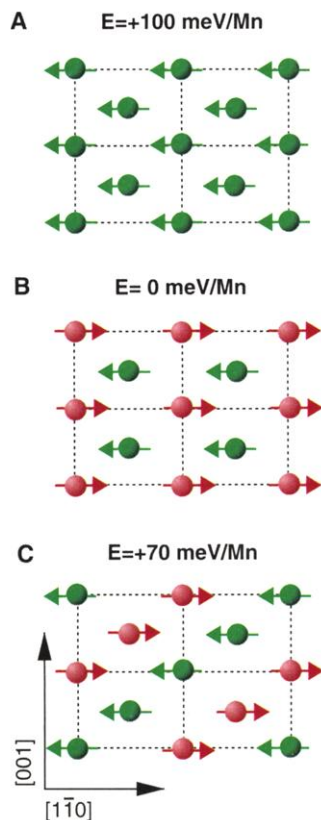


**Fig. 1.** Comparison of different magnetic configurations of the Mn ML on W(110): (A) the  $p(1 \times 1)$ -ferromagnetic structure, (B) the  $c(2 \times 2)$ -antiferromagnetic structure, and (C) the  $p(2 \times 1)$ -antiferromagnetic structure. The calculated magnetic moments are  $2.40 \mu_B$ ,  $\pm 2.96 \mu_B$ , and  $\pm 2.79 \mu_B$  for (A), (B), and (C), respectively. The total energies are given with respect to the configuration in (B).

If we image Mn on W(110) with a nonmagnetic tip,  $I = I_0$ , all atoms are equivalent and the chemical unit cell is diamond shaped (Fig. 3A). The four smallest reciprocal lattice vectors of this cell, all related by symmetry operations, are displayed in Fig. 3B. The superposition of the four corresponding plane waves gives the expected STM topography (Fig. 3C). An antiferromagnetic superstructure lowers the translational symmetry, and the additional tunneling current due to spin-polarized electrons,  $I_p$ , is sensitive to the unit cell of the superstructure (Fig. 3D). Therefore, smaller reciprocal lattice vectors become accessible (Fig. 3E). Since these possess exponentially larger coefficients, they dominate the STM image,  $\Delta I \approx \Delta I_p$ , even in the case of small effective spin-polarization  $P_S P_T \cos\theta$ , e.g., if  $\theta$  is near to  $90^\circ$ . Thus, the corrugation amplitude  $\Delta z$  (the maximum difference in tip height while it scans the surface) is directly proportional to the spin-polarization,  $\Delta z(z_0) \sim P_S P_T \cos\theta$ , where  $z_0$  is the average tip-sample distance. Because of the smallest reciprocal superlattice vector, a stripe pattern (Fig. 3F) without any chemical background is expected to be seen in the experiment. Correspondingly, we expect a

diagonal stripe pattern for the  $p(2 \times 1)$ -AFM state (Fig. 1C). The arguments are quite general and are, in principle, applicable to any magnetic superstructure. The electronic structure, contained in  $I_{G_{\parallel}^{(1)}}(\theta, V)$  of Eq. 2, of a specific surface can still compete with this effect, and first-principles calculations were performed in order to interpret the experiments unambiguously. STM images were calculated on the basis of the Tersoff-Hamann model (14), an approach equally successful for semiconductor (15) and transition-metal surfaces (13, 16). The spin-polarized measurements derived from a ferromagnetic tip were simulated by assuming different values for the spin-polarization  $P_T$  of the tip states.

The SP-STM experiments were performed in a cryogenic ultra-high vacuum system equipped with a 2.5-T magnet (17) and separate chambers for substrate preparation, sample transfer, metal vapor deposition (MVD), and surface analysis. The sample preparation procedure is described in detail in (17, 18). We used etched W tips, which were flashed in vacuo to remove oxide layers. In the MVD chamber, the tips were magnetically coated with Fe or Gd at a temperature of 300 K, were subsequently

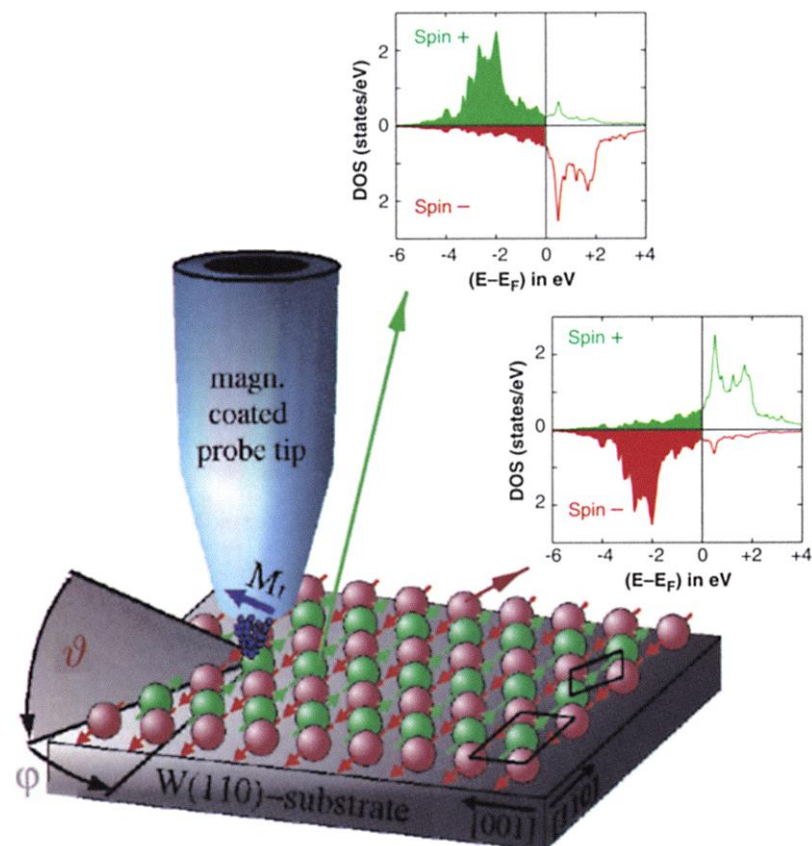


**Fig. 2.** Principle of spin-polarized scanning tunneling microscopy using a ferromagnetically coated probe tip that is scanned across a Mn ML film on W(110). The magnetic ground-state configuration is shown (Fig. 1) and the corresponding DOS of the ferro- (top graph) and antiferromagnetic (bottom graph) Mn atoms. The angle  $\theta$  between the magnetization axes of tip and sample can be related to  $\vartheta$  and  $\varphi$  by  $\cos\theta = \cos\varphi \cos\vartheta$ . Additionally, the diamond-shaped chemical unit cells and the rectangular magnetic unit cells are displayed.

annealed at  $T \approx 550$  K for 4 min, and then were transferred into the cryogenic STM. During the measurement, tip and sample were at a temperature  $T = 16$  K.

The growth of Mn on W(110) has previously been studied (18). It was found that a ML of Mn grows atomically flat and pseudomorphically on W(110); i.e., Mn has the same in-plane lattice constant as the underlying W substrate. No hints of alloying could be observed. The topography of 0.75 ML Mn/W(110), as grown at a substrate temperature  $T_{\text{sub}} \approx 400$  K (Fig. 4), shows atomically flat Mn islands as well as parts of the uncovered W substrate.

Using a clean W tip, atomic resolution was achieved on the Mn islands (Fig. 5A). The diamond-shaped unit cell of the  $(1 \times 1)$ -grown Mn ML is clearly visible. The line-section drawn along the dense-packed  $[1\bar{1}1]$  direction exhibits a periodicity of  $0.27 \pm 0.01$  nm, which almost perfectly fits the expected nearest-neighbor distance of 0.274 nm. The measured corrugation amplitude amounts to 15 pm ( $1 \text{ pm} = 1 \times 10^{-12} \text{ m}$ ). A calculated STM image for a conventional tip without spin-polarization, i.e.,  $P_T = 0$ , is given for comparison (Fig. 5A, inset). Obviously, the qualitative agreement between theory and experiment is excellent. However, the theoretically determined corrugation amplitude is by far too small. This deficiency of the Tersoff-Hamann model in predicting the correct corrugation in atomically resolved STM images of close-packed metal surfaces is well understood (19) and is related to the unknown atomic structure of the tip.

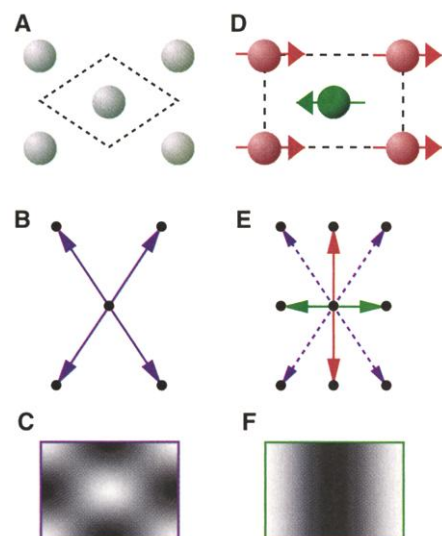


**Fig. 3.** Lattice (A and D), shortest reciprocal lattice vectors (B and E), and the expected STM images (C and F), associated to the shortest reciprocal lattice vectors of the chemical (left) and the magnetic (right) unit cell of a Mn ML on W(110). Note that (E) contains the shortest vectors of the chemical unit cell (dashed lines) and the two inequivalent pairs of additional vectors due to the magnetic superstructure.

In a second set of experiments, we used different ferromagnetic tips. Because we know from the first-principles computations that the easy magnetization axis of the Mn ML on W(110) is in-plane, the experiment required a magnetic tip with a magnetization axis in the plane of the surface in order to maximize the effects. This condition is fulfilled by Fe-coated probe tips (20). Figure 5B shows an STM image taken with such a tip. Periodic parallel stripes along the  $[001]$  direction of the surface can be recognized. The periodicity along the  $[1\bar{1}0]$  direction amounts to  $4.5 \pm 0.1$  Å, which corresponds well to the size of the magnetic  $c(2 \times 2)$  unit cell. The inset in Fig. 5B shows the calculated STM image for the magnetic ground state, i.e., the  $c(2 \times 2)$ -AFM configuration as discussed in Fig. 1B. We find that theory and experiment give a consistent picture. Even the predicted faint constrictions of the stripes along the  $[001]$  direction related to the pair of second smallest reciprocal lattice vectors of Fig. 3E are visible in the measurement. Again, experimental and theoretical data can be compared more quantitatively by drawing line-sections along the dense-packed  $[1\bar{1}1]$  direction (Fig. 5B). The result is plotted in Fig. 5C. It reveals that the periodicity, when measured with a Fe-coated probe, is twice the nearest-neighbor distance—i.e., 0.548 nm. The experimental corrugation amounts to 3 to 4 pm, which is slightly below the corrugation expected from theory (21),  $\Delta z(5\text{Å}) = 7$  pm.

The strong dependence of the effect on the magnetization direction of the tip can be exploited to gain further information on the magnetization direction of the sample by using a tip that exhibits an easy magnetization axis that is almost (22) perpendicular to the one of the sample surface. This condition is fulfilled by a W tip coated with  $7 \pm 1$  ML Gd, as we recently showed (23).

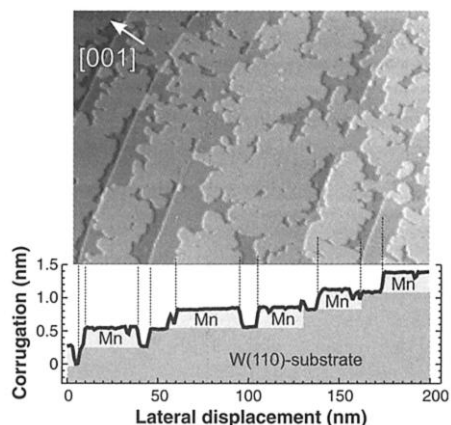


**Fig. 4.** Topography of 0.75 ML Mn grown on a stepped W(110) substrate. A line-section (bottom panel) was drawn at the bottom edge of the image. The structure of the sample is schematically represented by different gray levels. The image size is 200 nm by 200 nm.

In Fig. 5C, we included a typical line-section as measured with a Gd-coated probe tip (gray line). Indeed, the corrugation amplitude was always much smaller than that for Fe-coated tips and never exceeded 1 pm, thus supporting the theoretical results that the easy axis of the Mn atoms is in-plane. Note that the image still displays the stripe pattern characteristic of the magnetic superstructure, as proposed by the discussion of Eqs. 1 and 2; even for a small effective spin-polarization due to nearly orthogonal magnetization directions.

In conclusion, we present a direct proof of the predicted 2D antiferromagnetic state of a Mn ML film on W(110). Because it is able to resolve antiferromagnetism at the ultimate limit, SP-STM opens the door to the investigation of atomic-scale magnetism with complex magnetic structures.

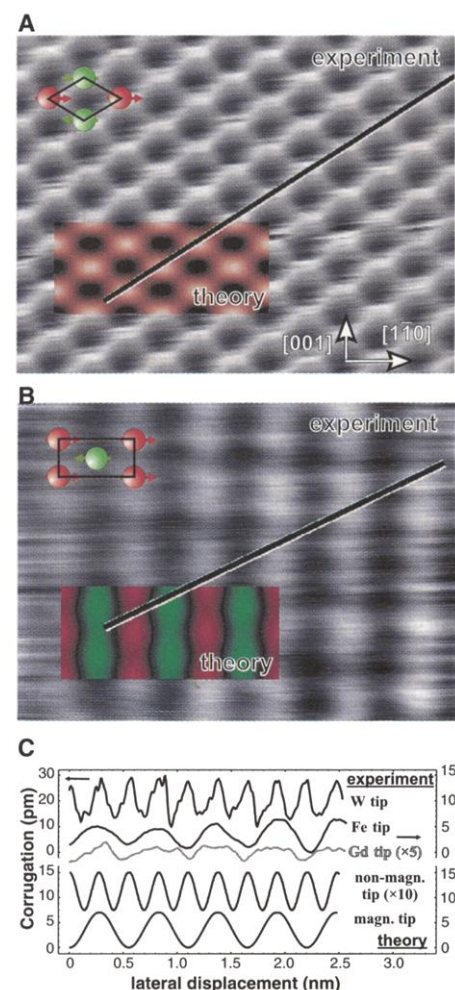


**Fig. 5.** Comparison of experimental and theoretical STM images of a Mn ML on W(110) with (A) a nonmagnetic W tip and (B) a magnetic Fe tip. (C) Experimental and theoretical line sections for the images in (A) and (B). The unit cell of the calculated magnetic ground-state configuration is shown in (A) and (B) for comparison. Tunneling parameters for both images are  $I_{\text{tun}} = 40$  nA and  $U = -3$  mV. The image size is 2.7 nm by 2.2 nm.

References and Notes

1. J. B. Kortright *et al.*, *J. Magn. Magn. Mater.* **207**, 7 (1999).
2. G. A. Prinz, *Science* **282**, 1660 (1998).
3. For a recent review, see J. Nogués and I. K. Schuller, *J. Magn. Magn. Mater.* **192**, 203 (1999).
4. H. A. Dürr *et al.*, *Science* **284**, 2166 (1999).
5. A. Scholl *et al.*, *Science* **287**, 1014 (2000).
6. S. Blügel, M. Weinert, P. H. Dederichs, *Phys. Rev. Lett.* **60**, 1077 (1988).
7. C. Krembel, M. C. Hanf, J. C. Peruchetti, D. Bolmont, G. Gewinner, *J. Magn. Magn. Mater.* **93**, 529 (1991).
8. P. Hohenberg and W. Kohn, *Phys. Rev. B* **136**, 864 (1964).
9. We used the density functional theory method, which is first-principles in that it requires no experimental input other than the nuclear charges. The FLAPW method is among the most accurate electronic structure methods, assuming no shape approximation to the charge density or potential. It is ideally suited to the problem of transition-metals in open geometry such as surfaces. Further, we use a film method with a semi-infinite vacuum, which provides a numerically excellent representation of states participating in the tunneling. No sensitivity of our results was found with respect to our choice of computational parameters, such as the number of  $k_{\parallel}$  (reciprocal lattice points used in 2D Brillouin-zone integrals) or basis-set sizes.
10. V. L. Moruzzi, J. F. Janak, A. R. Williams, *Calculated Electronic Properties of Metals* (Pergamon, New York, 1978).
11. R. Wiesendanger *et al.*, *Phys. Rev. Lett.* **65**, 247 (1990).
12. R. Wiesendanger *et al.*, *Science* **255**, 583 (1992).
13. S. Heinze, S. Blügel, R. Pascal, M. Bode, R. Wiesendanger, *Phys. Rev. B* **58**, 16432 (1998).
14. J. Tersoff and D. R. Hamann, *Phys. Rev. Lett.* **50**, 1998 (1983).
15. V. P. LaBella *et al.*, *Phys. Rev. Lett.* **83**, 2989 (1999).
16. S. Heinze, R. Abt, S. Blügel, G. Gilarowski, H. Niehus, *Phys. Rev. Lett.* **83**, 4808 (1999).
17. O. Pietzsch, A. Kubetzka, D. Haude, M. Bode, R. Wiesendanger, *Rev. Sci. Instrum.* **71**, 424 (2000).
18. M. Bode, M. Hennefarth, D. Haude, M. Getzlaff, R. Wiesendanger, *Surf. Sci.* **432**, 8 (1999).
19. A better quantitative agreement can be obtained by including more localized tip-orbitals such as  $d_{z^2}$ , whose corrugation amplitudes are much closer to the experiment in (13).
20. M. Bode, M. Getzlaff, R. Wiesendanger, *Phys. Rev. Lett.* **81**, 4256 (1998); *J. Vac. Sci. Technol. A* **17**, 2228 (1999).
21. In the calculation, we assumed the magnetization axes of the sample and the probe tip to be collinear, i.e.,  $\cos\theta = \pm 1$ , and a spin-polarization of the tip states  $P_t = 0.4$ . This value has been determined in earlier experiments (20). In the present experimental setup, the degree of alignment cannot be controlled and, in principle, it can be noncollinear, which might explain the discrepancy between theory and experiment.
22. The in-plane or out-of-plane magnetization direction of tips coated by thin films is governed by the interface and surface anisotropy of the film material, i.e., Fe or Gd, in contact with the most densely packed W surface, i.e., W(110), which is formed at the tip apex after the thermal flash. To our experience, slight deviations from the ideal magnetization directions were frequently observed, probably caused by the local atom morphology of the tip.
23. O. Pietzsch, A. Kubetzka, M. Bode, R. Wiesendanger, *Phys. Rev. Lett.* **84**, 5212 (2000).
24. Financial support from the Deutsche Forschungsgemeinschaft (grant Wi 1277/6 and Bl 444/1-1), from the German-Israeli Foundation (grant I-550-184.14/97), and from the Bundesministerium für Bildung und Forschung (grant 13N7647) is gratefully acknowledged.

29 February 2000; accepted 25 April 2000

# A Nanoplotter with Both Parallel and Serial Writing Capabilities

Seunghun Hong and Chad A. Mirkin\*

The development of an eight-pen nanoplotter capable of doing parallel dip-pen nanolithography (DPN) is reported. Because line width and patterning speed in DPN are independent of contact force, only one of the tips in the parallel writing mode (the "imaging" tip) has a feedback system to monitor tip position and to write the pattern; all other tips reproduce what occurs at the imaging tip in a passive fashion. Proof-of-concept experiments that demonstrate eight-pen parallel writing, ink and rinsing wells, and "molecular corraling" via a nanoplotter-generated structure are reported.

The greatest limitation in using scanning-probe methodologies for doing ultrahigh-resolution nanolithography over large areas derives from the serial nature of most of these techniques. For this reason, scanning probe lithography (SPL) methods have been primarily used as customization tools for preparing and studying academic curiosities (1–9). If SPL methodologies are ever to compete with optical or even stamping lithographic methods for patterning large areas (10–12), they must be expanded to parallel processes. Several important steps have been taken in this direction. For example, researchers have developed a variety of different multiple-probe instruments for scanning (13–16), and some have begun to use these instruments for

parallel SPL. In particular, Quate and co-workers have shown that as many as 50 tips can be used at once (15), and with such a strategy, both imaging and patterning speeds could be dramatically improved. However, a major limitation of all parallel SPL methods thus far developed is that each tip within the array needs a separate feedback system, which dramatically increases the instrumentation complexity and cost. One of the reasons separate feedback systems are required in such processes is that tip-substrate contact forces influence the line width and quality of the patterned structures. Although parallel scanning tunneling microscope lithography has not yet been demonstrated, such a process would presumably require a feedback system for each tip that would allow one to maintain constant tunneling currents. Herein, we report a method for doing parallel or single-pen soft nanolithography using an array of cantilevers and a conventional atomic force microscope (AFM) with a single feedback system.

Recently, we invented a type of serial

SPL, called dip-pen nanolithography (DPN) (17–20), in which organic molecules ("inks"), which are cast onto an AFM tip, are deposited through a water meniscus (21) directly onto an underlying substrate. An ink that reacts with the substrate is often chosen so that the process will yield stable monolayer structures. The technique can be applied in general with many types of molecule-based inks (17–20), it works under ambient conditions, it offers 15-nm line-width resolution and 5-nm spatial resolution, and it can be done over relatively large areas in automated fashion. Moreover, others have shown that DPN can be merged with nanografting to increase the resolution of this lithography further for soft structures (22). However, as with most other SPL methods, DPN thus far has been used exclusively in a serial format. Finally, it is important to note that others have unsuccessfully attempted to use scanning-probe instruments to transport organic materials onto solid substrates to form stable nanostructures (23). It is, in part, the recognition of the existence of the meniscus (21) and the ability to use it as an ink transport medium under regulated humidity (17–20) that make controlled molecular writing on the nanometer-length scale possible.

All experiments were performed on a Thermomicroscopes M5 AFM, which is equipped with a closed-loop scanner that minimizes thermal drift. Custom nanolithography software was used to drive the instrument. The instrument has a 200-mm by 200-mm sample holder mounted on an automated translation stage. The details of serial, single-tip DPN writing and pattern alignment procedures have been described elsewhere (19). Our intention in transforming DPN into a parallel process was to create an SPL method that enables one to generate multiple, single-

Department of Chemistry and Northwestern University Center for Nanofabrication and Molecular Self-Assembly, Northwestern University, 2145 Sheridan Road, Evanston, IL 60208, USA.

\*To whom correspondence should be addressed. E-mail: camirkin@chem.nwu.edu